Lintong Cai

ATMO/OCN 665 term-project

Professor: Kelvin Richards

The Dispersive Properties of Langmuir Circulation

1. Introduction

The surfaces of lakes and oceans often exhibit arrays of convergence zones, which usually aligned to each other, and parallel to the surface wind direction (Fig. 1). These convergence zones are associated with roll cells caused by upwelling and downwelling motions in the near surface of ocean. Fig. 2 illustrates structure of LC, the counterrotating vortices induced by wind. This phenomenon was first described by Langmuir (1938) and bears his name now. Langmuir circulation (LC) plays a key role in transferring momentum and heat in the ocean surface boundary layer, which enhances air-sea exchange and mixing. Previous researches done by Craik and Leibovich in 1976 investigated the LC generation mechanism; the equations derived by them gives a clue on how to numerically model the LC, and the improved second generation is commonly used in LC simulation (Leibovich, 1977).

Fig. 1: Windrows comprised mainly of foam from breaking waves in the lake, Loch Ness. The surface convergence regions were marked as the Langmuir Circulation (Thorpe, 2004).

LC is a key contributor to vertical mixing and ocean dispersion, as it traps floating matter in narrow convergence zones at the surface (Thorpe, 2004). While dispersive processes can quickly redistribute the materials in the ocean over various scales from molecular to mesoscale. Previous studies attempt to give a comprehensive theoretical description on ocean dispersive processes (McWilliams, 2016; Kunze, 2019), but much problems are still unanswered, especially in the smaller scale over ocean boundary layer where is affected by many factors like complex interaction and other marine biological processes. Shrestha et al. (2018) studied the LC dispersive properties in Large-eddy simulation model. They reveal the relationship that increasing the Stokes drift velocity and decreasing surface wind stress both change the horizontal size of coastal Langmuir cells. Besides, wavenumber also contributes the horizontal extent of Langmuir cells.

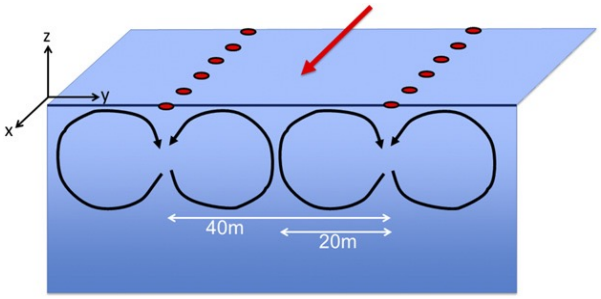

Fig. 2: Counterrotating Langmuir circulation cells of 20-m diameter with arrows indicating direction of rotation with wind direction shown by red arrow. Red plates are shown clustered in the convergence zones (above downwelling regions), which are spaced 40 m apart (Chang et al., 2019).

Ocean dispersion experiments with different tracers capture the ocean's dispersive characteristics directly, and the datasets can quantitative analysis these characteristics. However, these experiments pose technical challenges due to the limitation in both time and space scales since observed dataset must under fair accuracy. Chang et al (2019) using an innovative method (Carlson et al., 2018) by tracking floating bamboo plates from an aerostat tethered to a station-keeping ship. The brief introduction about the experiment is in the next section. As for the observational and reanalysis results will be mentioned in the section 3. The last section focuses the conclusions.

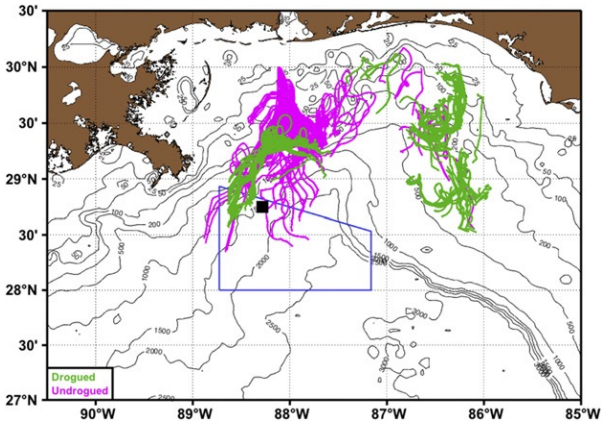

Fig. 3: Northeastern Gulf of Mexico with bathymetry contours. The blue box indicates the area where aerostat operations were permitted. Trajectories of GPS-tracked surface drifters with (green) and without (magenta) drogue from 1 Feb through 4 Feb 2016 are shown. The black square marks the location of the Langmuir experiment on 6 Feb 2016 near 28.75°N, 88.28°W (Chang et al., 2019).

2. Experimental setup

The experiment field is shown in Fig. 3. The trajectories of bamboo plates are chosen because it's cheap, biodegradable and positively buoyant with nominally no windage. The plates' diameter is 28cm and thickness of 2mm with 1.75cm draft. These plates are easy to be detected. Once they soak into water, the wind forcing is negligible. However, the observational window is limited by the time the camera can kept aloft with the plates,

and nighttime cannot capture the imageries. These limitations may cause some errors. After the boat tosses the bamboo plates, camera will take high-resolution images every 15 seconds. The large effort is required to track the plates visually and depict correct trajectories. In this case, the plates are painted with red, yellow and magenta to distinguish easily.

The plates are being tossed along two tracks perpendicular to the wind with no more than 8 minutes, forming a 150m (crosswind) × 30m (downwind) patch pretty uniformly (Fig. 6a). The results used to analysis is about 2.5h during the Langmuir event on February 6th, 2016.

The LC happens in low winds and onset when Reynolds number equals to 530±20 in a previously quiescent fluid (Thorpe, 2004). During the experiment period, wind speed was steady between 5 and 7 $m \cdot s^{-1}$ southward, and surface net flux decreased from slight heating to cooling (Fig. 4a). Potential density ρ profiles in Fig. 4b illustrated the mixed layer is about 40-50m. And the temperature profile at 16:37 as local time (CST) indicate an additional gradient at 20-30m depth, which corresponds to the dominant Langmuir cell diameter in the experiment.

As shown in Fig. 4c, the spectral averaged wave direction was about 30°, while the wind direction simultaneously measured on the weather stations on the two main vessels, the *R/V Walton Smith*, was about 0°.

The generation process of LC depends critically on the Stokes drift induced by surface waves and vorticity. Just briefly review on the generation process, the process can be formulated as one in which the flow forced by a wind stress τ, is characterized by a friction velocity $u_* = \sqrt{\tau/\rho}$, and ρ denotes density of ocean. The Stokes drift can be written as $U_s = 2S_0 e^{2\beta z}$. The Langmuir number, La is defined as

$$La = (\nu_T \beta / u^*)^{\frac{3}{2}} (S_0/u^*)^{-\frac{1}{2}} \tag{1}$$

Where ν_T is eddy viscosity, and S_0 as well as β can be estimated from the empirical Pierson-Moskowitz spectrum of surface waves,

$$2S_0 = (0.014 to 0.015) W_{10} \tag{2}$$

$$\beta^{-1} = 0.24 W_{10}^2 / g\,. \tag{3}$$

Then u_* lies in the range $(1.05\ to\ 1.54) \times 10^{-3} W_{10}$, and W_{10} denotes the wind speed at the standard height of 10m above the water surface.

Although the equation above is pretty accurate, the difficult is choosing an appropriate turbulent eddy viscosity ν_T. To better solve this problem, Leibovich (1977),

McWilliams et al. (1997) defined a new parameter, turbulent Langmuir number, to better estimated from observations.

$$La_{turb} = u^*/U_s \tag{4}$$

The average Stokes drift profile is shown in Fig. 4d, which is collected by *R/V Walton Smith*. With a Stokes drift at the surface of $U_s = 4.67 \pm 0.49\ cm \cdot s^{-1}$, the turbulent Langmuir number $La_{turb} = 0.38 \pm 0.03$, the value indicates the condition is conducive to Langmuir turbulence.

3. experiment results

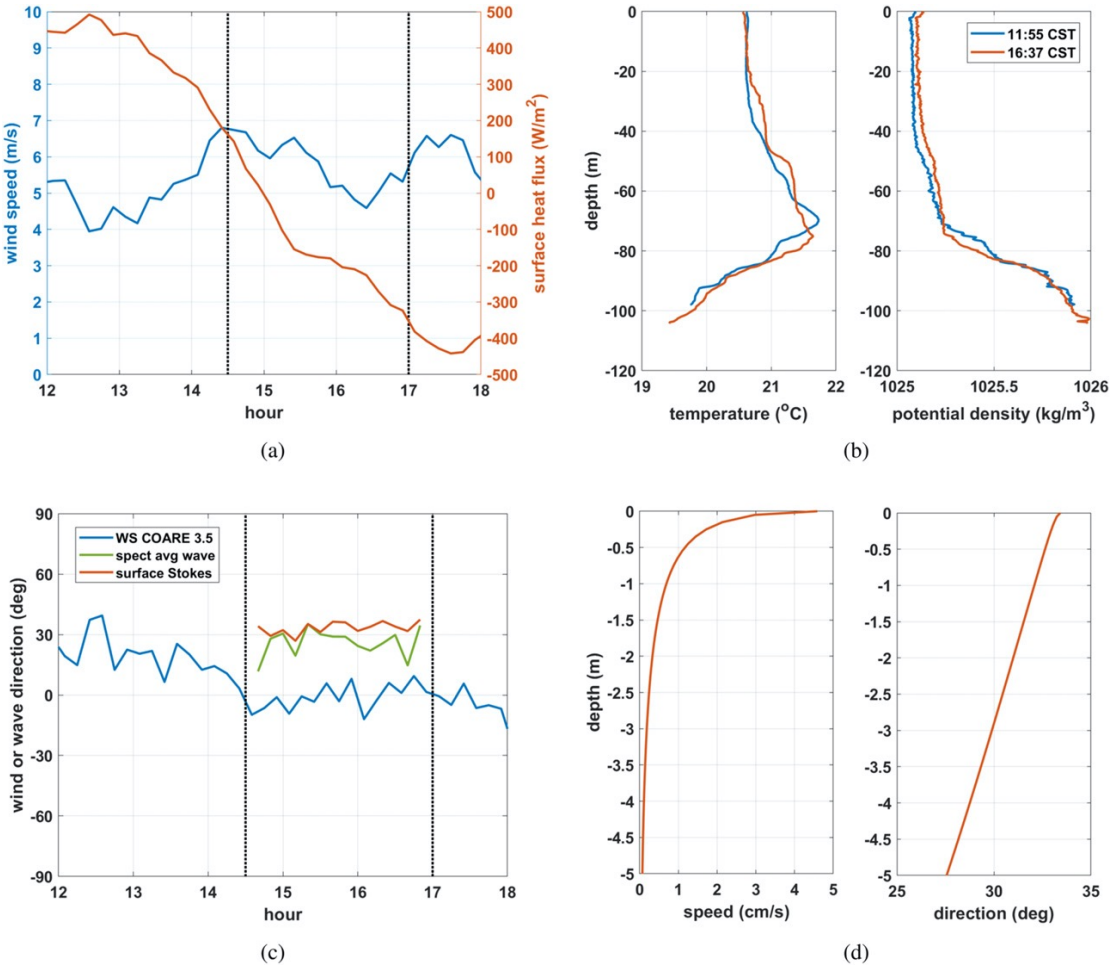

Fig. 4: Environmental conditions on 6 Feb 2016. (a) Wind speed (blue) and surface heat flux (red). (b) CTD temperature and potential density profiles. (c) Wind direction (blue); spectral averaged wave direction (green) and surface Stokes drift (red) based on wave buoy data. Start and end times of plate observations are indicated in (a) and (c) by black dotted lines. (d) Stokes drift speed (left) and direction (right) calculated from wave buoy data, averaged over the 2.5 h of the Langmuir experiment. Directions are reported as where wind, waves, and Stokes drift originate from (Chang et al., 2019).

a. Observations results

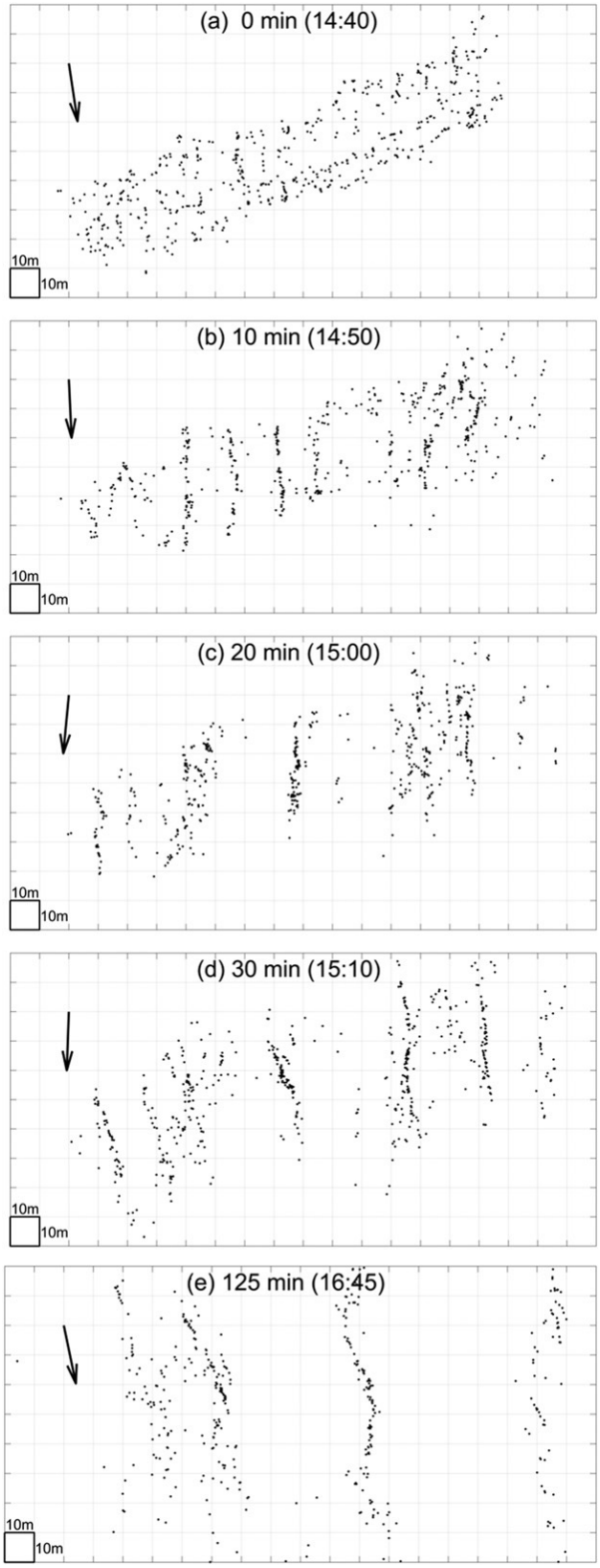

Fig. 5: (a)–(e) Relatively rectified plate positions after 0, 10, 20, 30, and 125 min, respectively. Black arrows show wind direction inferred from the heading of the aerostat, which was designed to point into the wind. Grid spacing is 10m in both directions. An animated version of this figure is included as online supplemental material (Chang et al., 2019).

Five snapshots of the redistributed plates are shown in Fig. 5. The plates are deployed uniformly at first. The convergence zones spacing around 15m with each other are clear to find after 10 minutes in Fig. 5b. Another 10 minutes, some windrows get closer and merge together. Another words, the spacing between each convergence zones becomes larger (40m) after 20 minutes.

This rapid spacing changing from 15m to 40m is just over 10 minutes. This secondary merging proves that LC is composed of the superposition of many scales of motion, resulted in the dominant LC cell diameter is 20m, meaning the 40-m spacing. Moreover, the initial spacing after the first 10min reveals smaller scale LC and after 20min a stronger, larger-scale LC induces a larger spacing with 40m.

Thereafter, the spacing in Fig. 5d remains the same as 20-min results. After 125min (Fig. 5e), convergence zones slightly separated more (50m). This final slow spacing increase in the spacing coincides with the transition with from surface net heating to cooling in the afternoon (Fig. 4a). This long lasting 40-50m scale implies the dominant LC cell diameter is 20-25m, which can be seen in the temperature profile at 16:37 CST in Fig. 4b, a gradient at 20-30-m depth. Besides the crosswind processes, the windrows grow from 30m at the beginning to 100m. Apparently, the dispersion is anisotropic.

The spatial data density analysis gives us more information on surface winds. Fig. 6 shows profiles of cumulative

plate count, average crosswind velocity, and average downwind velocity as functions of crosswind position at both early and late times. Early time results show a sinusoidal-like crosswind velocity v, and high plate accumulation regions are aligned where $\partial v/\partial y < 0$. Unlike the crosswind velocity, the downwind velocity almost shows no discernible pattern during the first 10min.

The distribution of plates become denser, and few plates are outside the convergence zones in later time.

Crosswind velocity experiences persistence strength with 1-2 $cm \cdot s^{-1}$ mean speed. However, the peak positive velocity of downwind roughly aligned with the convergence zones, while sometimes with little displacement. The displacement could be a consequence of the windrows tilted relative to instantaneous wind direction.

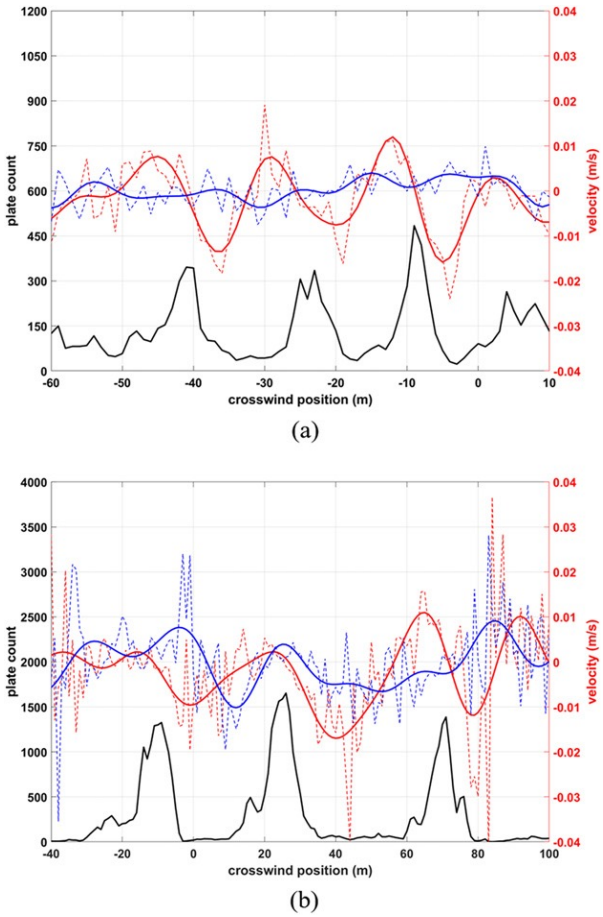

Fig. 6: Binned cumulative plate count (black), average crosswind velocity (red dashed), and average downwind velocity (blue dashed) as functions of crosswind position, for (a) the first 10min and (b) 50–90 min. The corresponding solid curves are low-pass-filtered velocities, with cutoff at 10 m for (a) and cutoff at 20 m for (b) (Chang et al., 2019).

b. Relative dispersion

Relative dispersion is in variant to translation and rotation of the plate field. The downwind RD_x and crosswind RD_y components are defined as

$$RD_x(t; l_{0_x}) = < [x_i(t) - x_j(t)]^2 >, \quad (5)$$

$$RD_y(t; l_{0_y}) = < [y_i(t) - y_j(t)]^2 >, \quad (6)$$

Where x_i are the plate positions, $<\cdot>$ denotes an average over all plate pairs, $i \neq j$, $l_{0_x} = \sqrt{< [x_i(t_0) - x_j(t)]^2 >}$ and $l_{0_y} = \sqrt{< [y_i(t_0) - y_j(t)]^2 >}$ are the initial separation scales in the downwind and crosswind directions, respectively.

Fig. 7 shows RD (black) averaged over all directions and scales, increases with time. Given the fact that the dispersion is pronounced anisotropic, the downwind RD_x component (blue) and crosswind counterpart are shown with different initial separation scales, $l_{0_x} = l_{0_y} = (2.3, 7.8, 15)m$. Crosswind relative dispersion grows much faster

than the downwind component when the initial separation scales is no less than the observed, short-time Langmuir cell size (about 7m). However, crosswind component saturates eventually at all initial separation scales. Meanwhile, downwind component grows slowly at first, after about 25min, all curves increases significantly. Chang et al. (2019) point out at these time scales, the downwind dispersion grows like $RD{\sim}t^2$, rather than the classic Richardson $RD{\sim}t^3$ prediction, indicating significant contributions from a mean shear component.

c. Two-point velocity statistics

Two-point method is a good way to determine the mean velocities with high accuracy. For plates i and j, the separation vector is given by

$$\boldsymbol{r}_{ij}(t) = \boldsymbol{x}_i(t) - \boldsymbol{x}_j(t). \qquad (7)$$

In this case, the relative velocity can be given as

$$\boldsymbol{\delta v_{ij}}(t) = \boldsymbol{v}_i(t) - \boldsymbol{v}_j(t) = \frac{d}{dt}\boldsymbol{r}_{ij}(t). \quad (8)$$

The longitudinal relative velocity component is defined as

$$\delta v_l = \boldsymbol{\delta v} \cdot \hat{\boldsymbol{r}}, \qquad (9)$$

and this is made up of both downwind and crosswind components. The transverse component is $\delta v_t = ||\boldsymbol{\delta v} \times \hat{\boldsymbol{r}}||$. Just like the relative dispersion, the longitudinal velocity increment δv_l is invariant to translation and rotation of the plate fields. The normalized probability density function (PDFs) of the longitudinal velocity increments at different separation r length-scales is shown in Fig. 8, whose normalization is with respect to the standard deviations (4, 5, and 6 $cm \cdot s^{-1}$ for separation at 0-20, 40-60, and 80-100m, respectively). It's clear that all the PDFs exhibit Gaussian cores with smaller scales exhibiting larger relative tails, which is consistent with large scales experiment done by Poje et al. (2017).

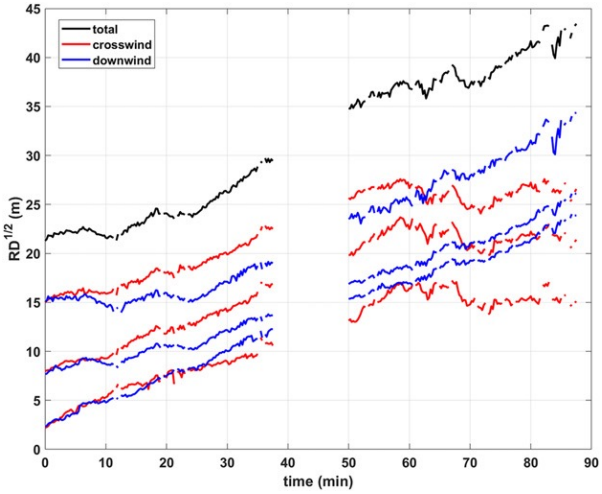

Fig. 7: Relative dispersion as a function of time for initially isotropic pair distributions. Average over all directions and scales (black), in the crosswind direction (red), and in the downwind di- rection (blue). Gaps reflect frames that could not be successfully processed (Chang et al., 2019).

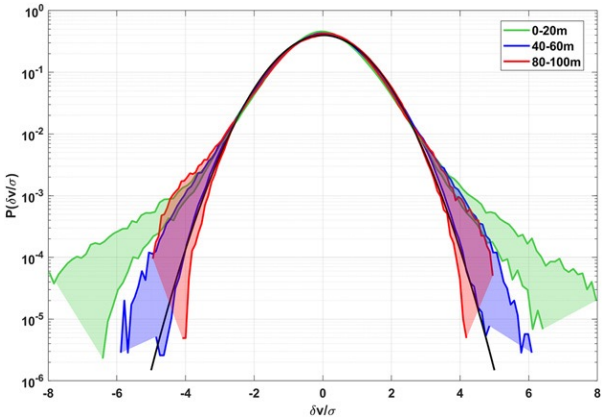

Fig. 8: Normalized PDFs of longitudinal velocity increments for three separation distance bins. Uncertainty is shown (shading) for maximum linking distances of 1.7–3.4m, which correspond to maximum velocities of 11–22 $cm \cdot s^{-1}$ relative to the mean. A normalized Gaussian is indicated by the black curve (Chang et al., 2019).

d. Structure functions

Longitudinal structure functions, are defined as

$$S_l^p(r) =< (\delta v_l)^p >, \tag{10}$$

and the moments of the longitudinal velocity increment. Fig. 9 and 10 show the first-order and second-order longitudinal structure functions, respectively.

The smallest separation is 0.7m, with each successive bin center increased by $\sqrt{2}$, up to when $r = 125m$. Data for smaller bins cannot be obtained reliably, since the separation distances should be larger than plate's diameter. Meanwhile, data for larger bins is also questionable because of sampling got from the edges of the experiment field. Bins with less than 8 pairs per time step also removed from the results.

The first-order structure function S_l^1 is the mean relative velocity as a function of separation r. Negative values indicate the flow tends to convergent, while positives values suggest divergent tendency of the flow. Since the surface velocity of LC is neither nondivergence nor homogeneous, first-order structure function $S_l^1 \neq 0$.

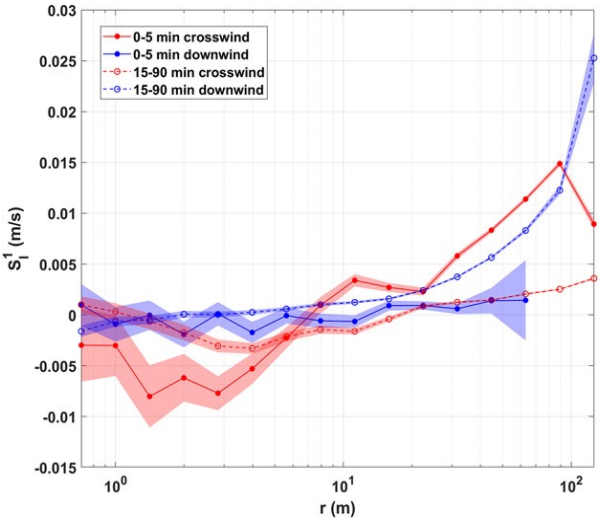

Fig. 9. Longitudinal first-order structure function for crosswind (red) and downwind (blue) components, subsampled at early (solid) and late (dashed) times. Shaded regions are 95% confidence intervals determined from standard error calculations (Chang et al., 2019).

In Fig. 9, the first-order structure function S_l^1 are drawn at early times (0-5min, solid curves) and later times (15-90min, dashed curves). Besides, the crosswind and downwind components are indicated by red and blue curves, respectively.

The early time crosswind component indicates mean convergence for separations below 7m, the LC cell diameter, and divergence at larger scales, which is consistent with the first observed windrow spacing of 15m (Fig. 5b). As for later times, the dashed red curve indicates zero crossing occurs at $r \approx 20m$, consistent with larger scale of LC cell diameter at later time. The averaged crosswind relative velocity is greater at early times when the plate distribution is more homogeneous.

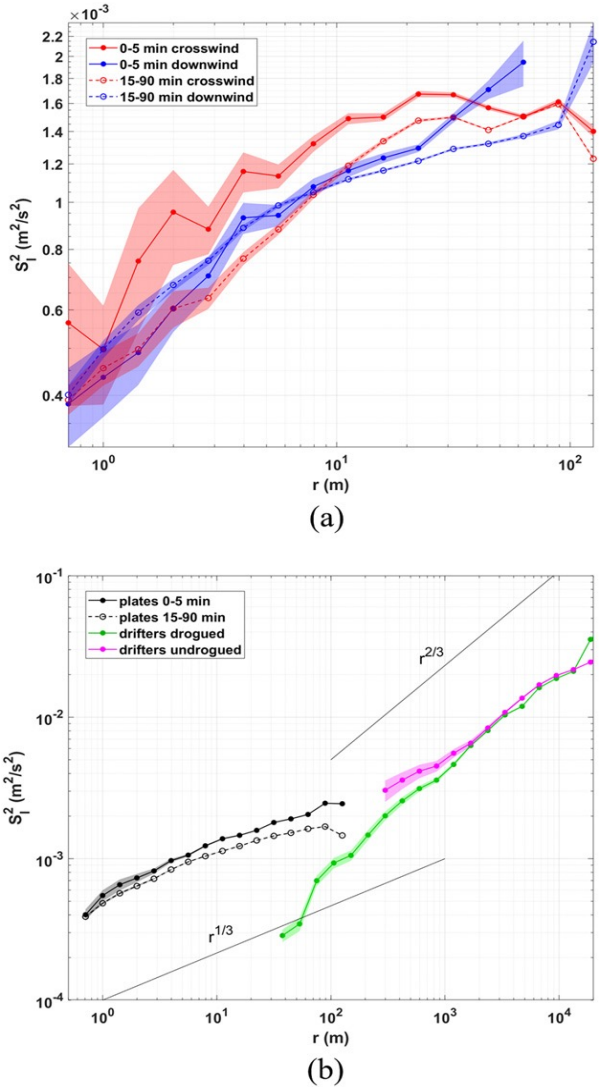

Fig. 10: Longitudinal second-order structure function. (a) Crosswind (red) and downwind (blue) components, subsampled at early (solid) and late (dashed) times. (b) For early time (solid black) and late time (dashed black) plates, plus drogued (green) and undrogued (magenta) drifters. Shaded regions are 95% confidence intervals determined from standard error calculations (Chang et al., 2019).

In contrast, there is no significant trend in the downwind direction at initial times (solid blue curve), although a clear mean divergence is shown at later times, rapidly increasing with the separation distance. This pattern matches the analysis results in Fig. 6. The strong anisotropy between the mean crosswind and downwind divergence at later times is also consistent with the slower growth in crosswind relative dispersion compared with downwind relative dispersion in Fig. 7.

The second-order structure function can describe the inertial range behavior of homogeneous isotropic turbulence. Fig. 10a shows that S_l^2 is higher in crosswind direction at early times than that of later times. In this case, the initial strong relative motion organizes the plates into Langmuir convergence zones. Moreover, the disparity arises over almost all scales, suggesting that LC consists of a superposition of motions from submeter to tens of meters. This support the theory described by Langmuir (1938), the hierarchy of LC vortices of different sizes.

The second structure function S_l^2 also shows differences between downwind and crosswind direction, especially at early times. While at later times, the LC cells suppress relative motion on scales less than

half their diameter, the evidence is that the downwind S_l^2 component exceed the crosswind component at these scales.

Chang et al. (2019) also calculated $S_l^2(r)$ from GPS-tracked surface drifters during a calm 3-day period before the plate experiment, to better connect the observations with larger scale dynamics. The additional experiment covered a larger range in the ocean. Fig. 10b contrast S_l^2 calculated by the drifter data and plate data.

At the largest scales in Fig. 10b ($r > 5km$), both drogued and undrogued drifters have roughly standard $S_l^2(r) \sim r^{\frac{2}{3}}$ scaling. While $r < 1-2km$, the drogued and undrogued drifter results diverge, with a shallowing slope of undrogued drifters, consistent with early time plate results at the largest scales of the plate experiment. Unlike the drifters drogued, the undrogued drifters and plates exhibit shallower remarkably, $S_l^2(r) \sim r^{\frac{1}{3}}$, scaling at small separation scales. Plates and undrogued drifters are more easily affected by shears and wave-induced motion at the very near surface, moreover, the undrogued drifters are greatly affected by direct windage.

The 2/3 power from the drogued drifters is consistent with the inertial range of a forward energy cascade in 3-dimensional turbulence in the theory of Kolmogorov.

5. Summary and discussion

Langmuir circulation is an important topic in the boundary layer. McWilliams et al. (1997) examined the roles of Langmuir circulation, and found that under typical wind and wave conditions, LC can significantly alter mean velocity and momentum flux profiles, greater anisotropy, and enhance turbulent velocity variance and skewness, dissipation, and entrainment buoyancy flux, compared to shear turbulence without LC. In this case, it is important to investigate the characteristics of LC, especially the aspect of dispersion.

Chang et al. (2019) set several small-scale dispersion experiments, which were performed using floating bamboo plates captured by a high-resolution camera mounted on a helium-filled aerostat over northern Gulf of Mexico during January-February 2016. These experiments are pretty straight forward and got sufficient great data to analysis. Individual plates were detected and linked to extract their velocities on separation scales of 1-100m. The statistics derived from the large number of plates show obvious differences between the downwind and crosswind directions. In the crosswind direction, plates spread out on average at scales larger than the dominant Langmuir cell diameters and converges at smaller scales. While in the downwind direction, spreading rate increases with separation distance, and this pattern is consistent with turbulent shear dispersion. Separation rate in downwind direction is remarkably larger than the crosswind counterpart at larger scales (Fig. 6) because of the constraining effect of LC. The crosswind component of second-order structure function is larger at early times,

implying Langmuir motions are active simultaneously at multiple scales. This supports the hypothesis that LC is composed of the superposition of many scales of motions, less likely the cells are growing over time.

As for the first-order structure function, the downwind component is relatively small over all scales at early times, but increases significantly with separation scales.

The additional experiment prior to the plates one, extends the results to larger scales, and compare the differences between near-surface and deeper depth. At scales less than 1km, the second-order structure function curves obtained from drogued drifters at 0.5-m depth and undrogued drifters as well as plates at 1-5cm depths diverge. The structure function at very shallow depths(1–5-cm) shows a shallower slope and more energy. This is likely that energy input from wind and waves alter the magnitude and slope of second-order structure function at small scales and shallow depths, which means extrapolation from mesoscale and submesoscale dispersion properties may not describe properly what happen at the small scales.

This kind experiments provides unique view to look at the motions, whose results can directly be compared with model simulations. Such comparisons reveal the defects of models and are very helpful to unravel the dynamics of small scales motions. The work by Chang et al. gives me deep impression and emphasis although model simulation is useful to analysis without many other influencers, field experiments are also critical since which show real processes in the world. The more important thing is to set up sophisticated experiments and rule out unnecessary factors. Such experiments are expected to lead to improved understanding of small scales motions and be improved with technical evolution.

Reference

Carlson, D. F., Özgökmen, T., Novelli, G., et al. (2018). Surface Ocean Dispersion Observations From the Ship-Tethered Aerostat Remote Sensing System. *Frontiers in Marine Science*, *5*. https://doi.org/10.3389/fmars.2018.00479

Chang, H., Huntley, H. S., Jr., A. D. K., et al. (2019). Small-Scale Dispersion in the Presence of Langmuir Circulation. *Journal of Physical Oceanography*, *49*(12), 3069–3085. https://doi.org/10.1175/JPO-D-19-0107.1

Kunze, E. (2019). A Unified Model Spectrum for Anisotropic Stratified and Isotropic Turbulence in the Ocean and Atmosphere. *Journal of Physical Oceanography*, *49*(2), 385–407. https://doi.org/10.1175/JPO-D-18-0092.1

Langmuir, I. (1938). Surface Motion of Water Induced by Wind. *Science*, *87*(2250), 119–123.

Leibovich, S. (1977). On the evolution of the system of wind drift currents and Langmuir circulations in the ocean. Part 1. Theory and averaged current. *Journal of Fluid Mechanics*, *79*(4), 715–743. https://doi.org/10.1017/S002211207700041X

McWilliams, J. C. (2016). Submesoscale currents in the ocean. *Proceedings: Mathematical, Physical and Engineering Sciences*, *472*(2189), 1–32.

McWilliams, J. C., Sullivan, P. P., & Moeng, C.-H. (1997). Langmuir turbulence in the ocean. *Journal of Fluid Mechanics*, *334*, 1–30. https://doi.org/10.1017/S0022112096004375

Poje, A. C., Özgökmen, T. M., Bogucki, D. J., & Kirwan, A. D. (2017). Evidence of a forward energy cascade and Kolmogorov self-similarity in submesoscale ocean surface drifter observations. *Physics of Fluids*, *29*(2), 020701. https://doi.org/10.1063/1.4974331

Shrestha, K., Anderson, W., & Kuehl, J. (2018). Langmuir Turbulence in Coastal Zones: Structure and Length Scales. *Journal of Physical Oceanography*, *48*(5), 1089–1115. https://doi.org/10.1175/JPO-D-17-0067.1

Thorpe, S. (2004). Langmuir circulation. *Annual Review of Fluid Mechanics*, *36*, 55–79. https://doi.org/10.1146/annurev.fluid.36.052203.071431.